Semnan University

Progress in Physics of Applied Materials

journal homepage: https://ppam.semnan.ac.ir/

Porosity and morphology control of mesoporous Cu-BTC Metal-Organic Framework microparticles

Kobra Vazirinezhad[a], Fatemeh Shariatmadar Tehrani[a]*, Sedigheh Zeinali[b]

[a] *Faculty of Physics, University of Semnan, P.O. Box 35195-363, Semnan, Iran*
[b] *Nanochemical Engineering Department, Faculty of Advanced Technologies, Shiraz University, Shiraz, Iran*

ARTICLE INFO

Article history:
Received: 19 February 2024
Revised: 1 March 2024
Accepted: 2 March 2024

Keywords:
Metal-Organic Framework
Solvent
Molar ratio of metal to ligand
Morphology
Porosity

ABSTRACT

In this study, Cu-BTC structures, one of the most widely used metal-organic frameworks (MOF), were synthesized by solvothermal technique, and the effect of metal-to-ligand ratio and the solvent content on their crystalline structure, chemical bonding, morphology, and porosity properties was investigated systematically by X-ray diffraction (XRD), field emission scanning electron microscopy (FESEM), Fourier transform infrared (FTIR) spectroscopy, and N_2 adsorption-desorption measurements, respectively. The results demonstrate that the metal-to-ligand molar ratio although does not noticeably affect the crystalline nature of the product, but observably controls the morphology so that spherical to octahedral microparticles can be achieved. In addition, the specific surface area (SSA) and total pore volume of the mesoporous structures are significantly enhanced to 969.5 m^2g^{-1} and 0.41 cm^3g^{-1}, respectively, for a 1:1 molar ratio of metal to ligand. On the other hand, changing the solvent content greatly increased the SSA (1364.8 m^2g^{-1}) and total pore volume (0.561 cm^3g^{-1}) by ~41% and ~37%, respectively. This would be promising finding for wide range of applications requiring high SSA materials.

1. Introduction

Metal-organic frameworks (MOFs) are materials with a long-range ordered crystalline porous structure made of organic linkers and metal clusters. The outstanding characteristics of these compounds are their tunable pore size, high specific surface area (SSA), low-density, good biocompatibility, and high adsorption. Therefore, MOFs are utilized in many different fields, such as sensing, drug delivery, gas storage, gas separation, catalysis, and supercapacitors, etc. [1-3]. Many experimental factors like pH, temperature, solvent type, molar ratio of metal to ligand, pressure, etc, affect the synthesis of MOFs [4-13]. Choosing a specific model for the factors that influence the synthesis of MOFs is one of the challenges that researchers have not yet solved.

The selection of metal-to-ligand ratio and solvent are very important parameters. So, the synthesized samples of MOF demonstrate that altering the molar ratio of metal-to-ligand results in modifications to the sample's SSA as well as its dimensions. On the other hand, solvents are involved in the formation and regulation of various coordination environments. So, rational selection of reaction solvents is a big challenge in MOFs structure formation. They have an impact on the coordination behavior of the metal and ligand, either directly or indirectly [14]. During the assembly process, solvents may function in concert with metal ions or appear as guests in the final network configuration. The majority of solvents can function as a medium for the crystal growth process or as an agent that directs structure, even though they might not be used in MOF synthesis [15]. Therefore, Due to the solvent's polarity and the organic linker's initial characteristics, the reaction environment affects the MOF synthesis process. As reported, different solvent systems exhibit varying morphologies under identical conditions all through the MOF synthesis process.

* Corresponding author.
E-mail address: *f tehrani@semnan.ac.ir*

Cite this article as:
Vazirinezhad, K., Shariatmadar Tehrani, F., Zeinalib, S., 2024. Porosity and morphology control of mesoporous Cu-BTC Metal-Organic Framework microparticles. *Progress in Physics of Applied Materials*, 4(1), pp.47-58.DOI: 10.22075/PPAM.2024.33337.1090

This may occur due to differences in the degree of deprotonation of organic bonds in different solvent systems. In addition to the structure, different solvents lead to the synthesis of MOFs that differ in pore size. The size of the solvent molecule influences the change in pore size caused by various solvents [16]. However, by changing their volume ratio, the structure may change from zero-dimensional to three-dimensional. For example, with the hydrothermal synthesis of Mg-BTC, the structural dimensions of the sample were obtained by changing the type of solvent (water and ethanol) from a zero-dimensional structure (with water solvent) to a three-dimensional structure (with ethanol solvent). Therefore, it makes sense that the solvent will have a significant impact on how secondary structural units self-assemble [9, 17, 18].

One of the MOF materials studied by many researchers is Cu-BTC, which was first reported in 1999 by Chui et al [19] and it is also known as MOF-199 and HKUST-1. This Cu-based MOF materials consist of copper nodes and organic ligands (benzene-1,3,5-tricarboxylate, BTC), with each copper coordinated four oxygen atoms and a water molecule [20]. This framework has a high SSA and contains a bimodal pore size distribution, i.e., a large cage with a diameter of 9 Å and small pores with a diameter of 3.5 Å [21, 22] with a variety of applications in sensors [23, 24], gas separation [25], supercapacitors, catalysis [26], and gas storage (H_2, CH_4, and CO). In the past years numerous techniques for synthesis of Cu-BTC have been reported including conventional hydro/solvothermal [27-29], mechanochemical [30, 31], microwave-assisted and ultrasonic [32-34], Ionothermal method [35], and electrochemical synthesis methods [36, 37]. All these methods can significantly affect most of the physicochemical properties, such as crystallinity, specific surface area, morphology, and pore volume of the synthesized Cu-BTC material. As a result, selecting the appropriate synthesis method can be one of the key factors for choosing its application. However, the exact influence of all synthesis parameters on the physical and chemical characteristics of the synthesized Cu-BTC has not been explored yet. Specifically, although the role of metal-to-ligand molar ratio and solvent content in the precursor solution are reported as important factors to control properties of MOFs in solvothermal synthesis method, however, only few research works are available investigating this issue for Cu-BTC. In this paper, successful solvothermal synthesis of Cu-BTC structure is presented and the impact of metal-to-ligand molar ratio and the solvent content on the product properties such as morphology and porosity studied.

2. Materials and methods

2.1. Materials

All materials, including copper (II) nitrate trihydrate $Cu(NO_3)_2.3H_2O$ (99%), 1, 3, 5 benzene tricarboxylic acid (H_3BTC) (99%), were purchased from Sigma-Aldrich, ethanol (99.9%, Merck), DMF (99.8%, Alfa Acer), and deionized water (DI-water). No additional purification was required for any of the reagents.

2.2. Sample preparation

In this work, Cu-BTCs were synthesized via the solvothermal method. Typically, *x* mmol of $Cu(NO_3)_2{\cdot}3H_2O$ was dissolved in 20 mL DI-water and *y* mmol of H_3BTC was dissolved in a mixture of 20 mL DI-water and 40 mL ethanol (the values of *x* and *y* are specified in Table 1). These solutions were mixed and stirred for 30 minutes, then transferred into a 200 mL Teflon-lined autoclave and heated at 120°C for 16 h. After cooling naturally to room temperature, the product was separated by centrifugation, washed several times with ethanol and DI-water, and then dried at 75°C for 12h to obtain Cu-BTC-H1, Cu-BTC-H2, Cu-BTC-H3, and Cu-BTC-H4 samples. Next, to investigate the effect of the solvent used in the synthesis, a sample similar to Cu-BTC-H2 was prepared, but DI-water, ethanol, and DMF solvents were used. So the amounts of solvents are 25, 25, and 30 mL for DI-water, ethanol, and DMF, respectively. This sample is named Cu-BTC-H5.

Table 1. Molar ratios of metal to ligand used in the synthesis process of the samples.

Sample ID	$Cu(NO_3)_2{\cdot}3H_2O$: H_3BTC
Cu-BTC-H1	1.5:1
Cu-BTC-H2	1:1
Cu-BTC-H3	1:1.28
Cu-BTC-H4	1:1.8

2.3. Characterization

X-ray diffraction (XRD) patterns of the materials were recorded using a (Bruker German) diffractometer with Cu Kα radiation (λ = 0.15406 nm) in the 2θ range of 5-45°. FTIR analysis was done in the wavenumber range of 4000-400 cm^{-1} with an FTIR spectrophotometer (Perkin Elmer Spectrum 65) using Cu-BTC seeded potassium bromide (KBr) powder. The morphologies of the obtained materials products were characterized by FESEM (TESCAN VEGA3 and MIRA3 models). Nitrogen adsorption-desorption isotherms were measured at 77 K by using a Micromeritics Belsorp mini. The samples were degassed at 100 °C for 5 hours before analysis. The Brunauer–Emmett–Teller (BET) and Barrett–Joyner–Halenda (BJH) methods were used to determine the samples' SSAs, total pore volumes, and pore diameters.

3. Results and Discussion

3.1. Effect of metal-to-ligand molar ratio

XRD is used to identify the phase of crystals and their structure, and the results are displayed in Figure 1. The XRD patterns of all synthesized Cu-BTC samples exhibit sharp and high-intensity peaks indicating the high crystallinity of the synthesized samples. The presence of diffraction peaks at 2θ values of 6.68°, 9.5°, 11.64°, 13.49°, 17.42°, 19.04°, 20.2°, 25.91°, and 29.3° are in accordance with (200), (220), (222), (400), (511), (440), (442), (731), and (751) crystal planes, respectively, which confirm the formation of the Cu-BTC structure following previous reports [38, 39]. It is also clear from the XRD patterns that

the intensity of corresponding diffraction peaks increases with decreasing the metal-to-ligand ratio from Cu-BTC-H1 to Cu-BTC-H3. However, a further reduction in the ratio of metal to ligand from Cu-BTC-H3 to Cu-BTC-H4 led to the decrement of peak intensity. This indicates that one important variable controlling the Cu-BTC structure's crystalline quality is the metal-to-ligand ratio.

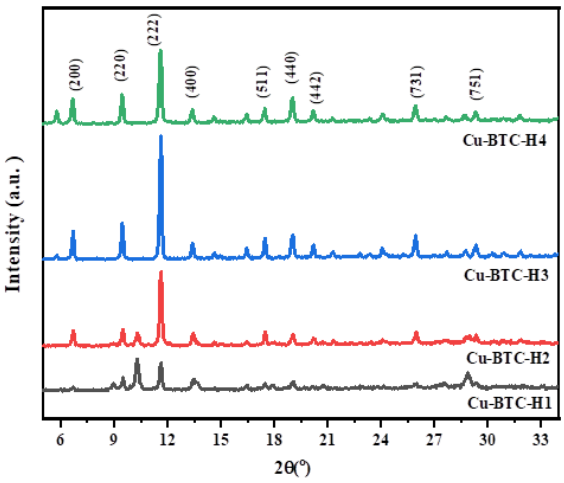

Fig. 1. XRD patterns of the samples of produced Cu-BTCs at various metal-to-ligand molar ratios.

To measure the average size of the crystals, two methods of Debye-Scherrer's equation (Eq. 1) and Williamson-Hall (W-H) equation (Eq. 2) have been used [40-42] and the achieved results are summarized in Table 2.

$$D_{Sh} = \frac{0.9\,\lambda}{\beta\,\mathrm{Cos}\theta} \quad (1)$$

Where D_{sh} is crystallite size, λ is the wavelength of $Cu_{k\alpha}$ radiation (1.5406 Å), β is the peak width at half maximum, and θ is the Bragg angle.

The results of calculating the average crystallite size of Cu-BTC samples from this method show that, by decreasing the metal-to-ligand molar ratio from Cu-BTC-H1 to Cu-BTC-H2, the crystallite size also decreases from 50.5 to 47.2 nm and then increases up to 52.3 nm for the sample Cu-BTC-H4, so that the sample Cu-BTC-H2 has the lowest crystallite size.

On the other hand, the effect of lattice strain (ε) in the samples due to defects and crystal distortion on the determination of crystallite size should also be considered, which is calculated using the W-H equation:

$$\beta\cos\theta = \frac{0.9\lambda}{D_{W-H}} + 4\varepsilon\sin\theta \quad (2)$$

To obtain the average crystallite size ($D_{W\text{-}H}$) and lattice strain using the W-H equation, βcosθ is plotted for all diffraction peaks against 4sinθ and the data points are fitted to a linear function. The slope and intercept of the fitting function give the lattice strain and average crystallite size, respectively. Figure 2 shows W-H plots of all the synthesized samples to calculate their crystalline properties. It should be mentioned that the values of R-squared (R^2) are greater than 0.92 for all samples, indicating that the linear function well fits the data. Table 2 reports the calculated values of lattice strain (ε) and average crystallite size (DW-H) for each sample. As expected, the values of $D_{W\text{-}H}$ are slightly higher than D_{sh}, however their variations follow a similar trend. Moreover, the strain of the samples decreases as the molar ratio of metal to ligands decreases from 1.5:1 to 1:1.28, but the lattice strain gradually increases with further decreases in the metal-to-ligand molar ratio. However, it is notable that the strain values obtained for all the samples are relatively low compared with other works [43].

The crystallinity percentage (Xc) of the samples, which refers to the degree of their structural order, is determined from XRD data using equation (3) [44]:

$$X_c = \frac{\sum_{i=1}^{i=n} A_{ci}}{At} \times 100 \quad (3)$$

where A_{ci} is the area under each diffraction peak with index i and A_t is the total area of the X-ray diffraction sub-pattern. The crystallinity% is shown in Table 2, which indicates a significant crystallinity enhancement with a reduction in molar ratio of metal-to-ligand from Cu-BTC-H1 to Cu-BTC-H3. But a further decrease in the molar ratio of metal-to-ligand leads to a lower crystallinity percentage. It can be noted that the variation in crystallinity percentage of the samples follows the reverse trend of their lattice strain changes. Therefore, the sample Cu-BTC-H3 has achieved the highest crystalline percentage and the lowest lattice strain, indicating its best crystalline quality among other samples.

The FTIR spectra of Cu-BTC samples are shown in Figure 3. The presence of almost identical absorption peaks in each sample's FTIR spectrum indicates the similar chemical nature of the samples, although some variations in the peak intensities are observed.

The peaks detected at 490 cm^{-1} and 730 cm^{-1} are attributed to the bending and stretching vibration modes of the Cu-O bond respectively [38, 45, 46]. The absorption peaks observed in the region of ~1108 cm^{-1} are due to C=O stretching vibrations [47]. The strong absorption peaks at 1373 and 1645 cm^{-1} are related to the stretching asymmetric and symmetric COO^- stretches of the 1, 3, 5 benzene tricarboxylic acid linkers respectively [48]. The absorption band at 1449 cm^{-1} was due to symmetric vibration modes of C=O, and broadband appearing at 3423 cm^{-1} is associated with the surface-absorbed water and hydroxyl groups in the Cu-BTC structure [49, 50]. The presence of the mentioned FTIR absorption peaks verifies that the Cu-BTC structure is successfully formed in all the samples, according to the references [47, 49, 51].

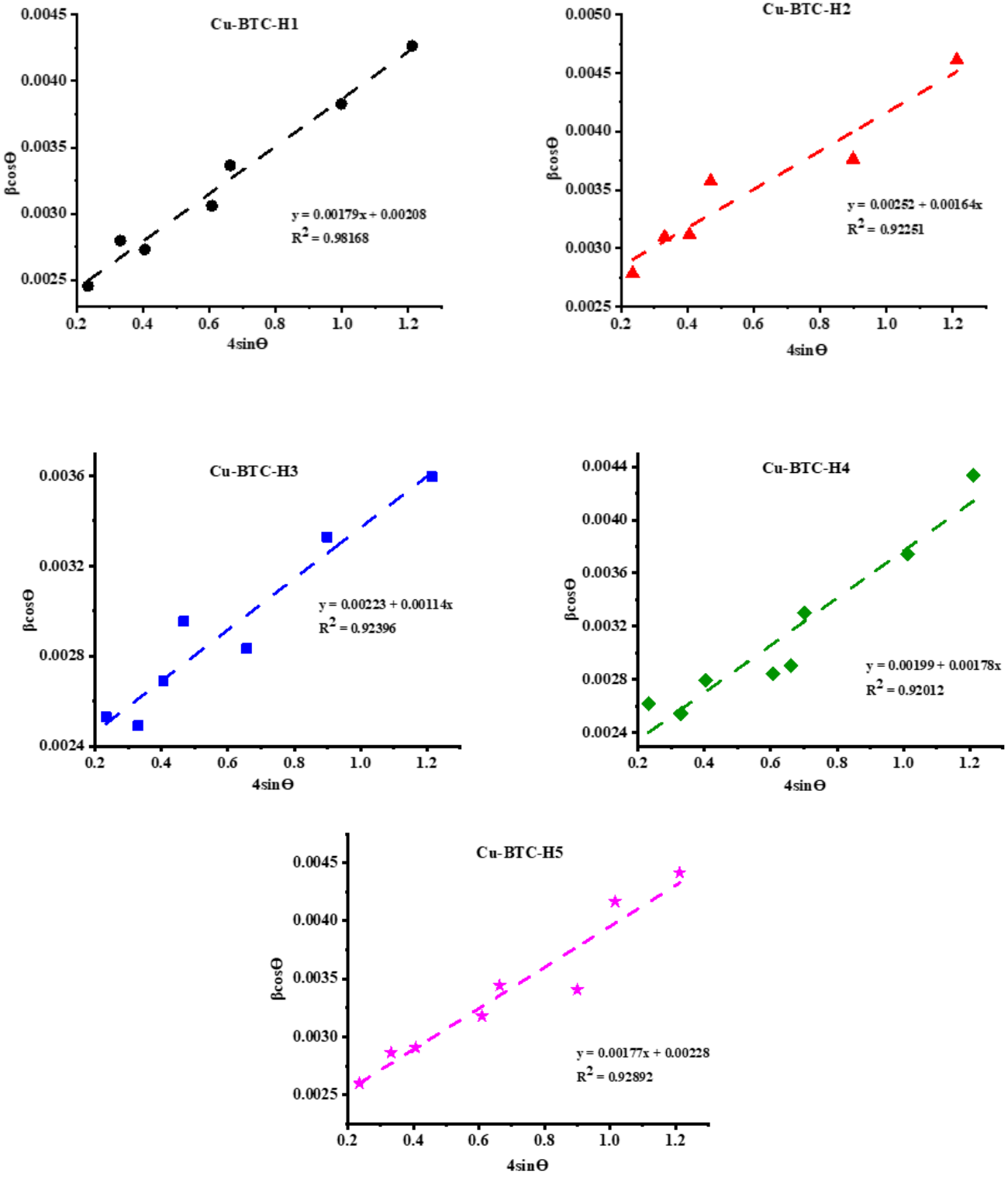

Fig 2. Williamson-Hall Plot for the samples Cu-BTC-H1, Cu-BTC-H2, Cu-BTC-H3, Cu-BTC-H4, and Cu-BTC-H5.

Table 2. Calculated crystalline properties of Cu-BTC samples obtained from XRD data.

Sample ID	D_{sh} (nm)	D_{w-h} (nm)	Lattice Strain	Crystallinity %	(222) peak position(2ɵ)	d-spacing (Å)
Cu-BTC-H1	50.5	66.7	0.0018	67	11.62	7.60
Cu-BTC-H2	47.2	55.1	0.0016	75	11.63	7.60
Cu-BTC-H3	51.6	62.2	0.0011	85	11.62	7.61
Cu-BTC-H4	52.3	69.7	0.0018	78	11.60	7.61
Cu-BTC-H5	49.8	60.3	0.0018	80	11.69	7.56

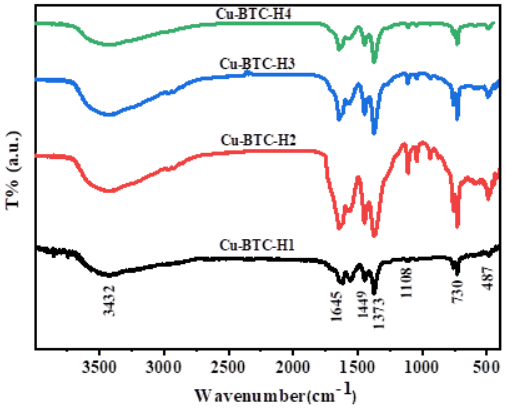

Fig. 3. FTIR spectra of Cu-BTC samples synthesized at various metal-to-ligand molar ratios.

FESEM analysis is used to study the morphology of the samples [52, 53]. Figure 4 shows the FESEM images reported at a 20- micrometers scale. In the case of the sample Cu-BTC-H1, where the molar ratio of metal to the ligand is the highest, spherical particles are formed. As the ratio of ligand to metal increases, the morphology of particles gradually evolves to rhombic polyhedral and the particle size becomes small. The particles size is measured by using Digimizer software, and the average particle size is determined as ~16.47 µm, ~15.42 µm, ~13.78 µm, and ~14.35 µm for Cu-BTC-H1, Cu-BTC-H2, Cu-BTC-H3, and Cu-BTC-H4, respectively. The histograms of particle size distribution of the samples are also demonstrated in Figure 4. As a result, molar ratio metal-to-ligand significantly controls the morphology and size of the formed particle. Luo et al. have synthesized Cu-BTC by ultrasonic method with molar ratios (H_3BTC: Cu^{2+} = 1:1.5 and 1:2), where a molar ratio of 1:2 leads to a high concentration of free Cu cations in the structure. This have led to poor kinetic control and the formation of particles with an uncertain morphology, but when the molar ratio selected as 1:1.5, the optimal values have been obtained by ball milling with the help of ultrasonic waves for 30 minutes [54]. In another study, Zhang et al. have mixed Co $(NO_3)_2$ with Hmim in a solution to create a new zeolite imidazole framework (ZIF-L-Co).

They changed the shape and phase of the samples by adjusting the reactant concentrations or molar ratios. The morphology changed from leaf-like sheets to rod-like structures when the metal-to-ligand molar ratio was raised from 8 to 24. This value was increased from 32 to 48, which smoothed out the rough polyhedron and made its edges and corners apparent [55].

To investigate the qualitative elemental analysis and the purity of the samples, the EDX analysis is performed. As expected, the C, O, and Cu elements present in the ligand and copper metal are identified and the trace of unwanted impurities is not detected. The EDX spectra for the samples synthesized at different metal-to-ligand molar ratios are reported in Figure 5. The atomic and weight percentages of the constituent elements are shown in Table 3. Also, a typical EDX mapping image of the Cu-BTC-H4 sample is depicted in Figure 6 which verifies the product's constituent elements' uniform distribution.

Figure 7a shows the measured Nitrogen adsorption-desorption isotherms for the samples. The isotherms are comparable to type I in accordance with the IUPAC classification indicating the porous nature of the synthesized products. The Cu-BTC-H1 sample has a mesoporous structure with a pore diameter of 2.17 nm, while the other samples have a microporous structure with pore diameters of less than 2 nm, based on the pore size distribution obtained from the BJH analysis method (Figure 7b). The results show that the Cu-BTC-H2 sample exhibits an obvious higher SSA of 969.5 m^2g^{-1} and pore volume of 0.41 cm^3g^{-1} than other samples. This evidently verifies the important controlling role of the metal-to-ligand molar ratio on the porosity properties of the synthesized Cu-BTC structure. Table 4 summarizes all samples' SSA, pore volume, and pore diameter.

Overall, the crystalline and chemical natures of Cu-BTC samples are not significantly affected by the change in the molar ratio of the metal-to-ligand, while it showed a notable influence on the crystalline quality and crystallite size, according to the results of XRD and FTIR analyses. FESEM and BET data, however, demonstrate that this parameter significantly affects the shape and porosity of the samples. Since the SSA can be regarded as one of the most important properties of MOF materials for various applications such as photocatalysts, gas sensing, and adsorption, Cu-BTC-H2 with the highest SSA among all samples is chosen and the impact of solvent composition on the properties of this sample is exclusively investigated and shown in the following section.

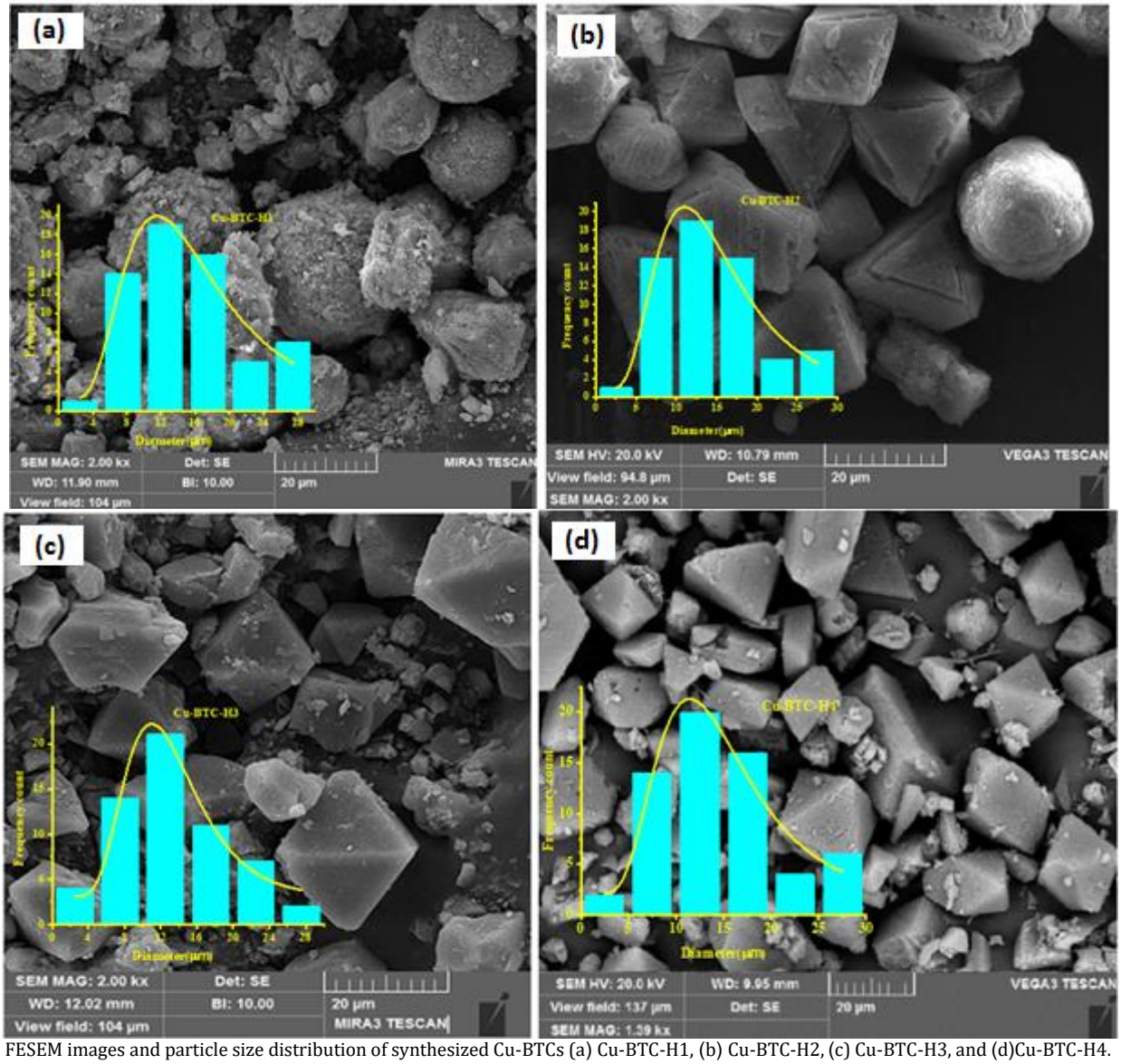

Fig. 4. FESEM images and particle size distribution of synthesized Cu-BTCs (a) Cu-BTC-H1, (b) Cu-BTC-H2, (c) Cu-BTC-H3, and (d)Cu-BTC-H4.

Table. 3. Elemental atomic and weight percentage in the Cu-BTC samples synthesized at different metal-to-ligand molar ratios.

Samples	Cu-BTC-H1		Cu-BTC-H2		Cu-BTC-H3		Cu-BTC-H4	
Element	Weight%	Atomic%	Weight%	Atomic%	Weight%	Atomic%	Weight%	Atomic%
C	34.22	60.28	26.27	42.09	32.62	47.26	36.41	60.42
O	18.00	23.81	39.53	47.55	42.13	45.83	21.06	26.24
Cu	47.78	15.91	34.20	10.36	25.25	6.92	42.53	13.34

Table 4. Selected porosity properties of the total Cu-BTC samples derived from Nitrogen adsorption- desorption measurement.

Sample ID	**Metal-to-ligand molar ratio**	**$a_{s,BET}$ (m^2g^{-1})**	**Total pore volume (p/p_0=0.988) (cm^3g^{-1})**	**BJH average pore diameter (nm)**
Cu-BTC-H1	1.5:1	216.9	0.11	2.17
Cu-BTC-H2	1:1	969.5	0.41	1.68
Cu-BTC-H3	1:1.3	634.8	0.26	1.65
Cu-BTC-H4	1:1.8	572.8	0.25	1.83

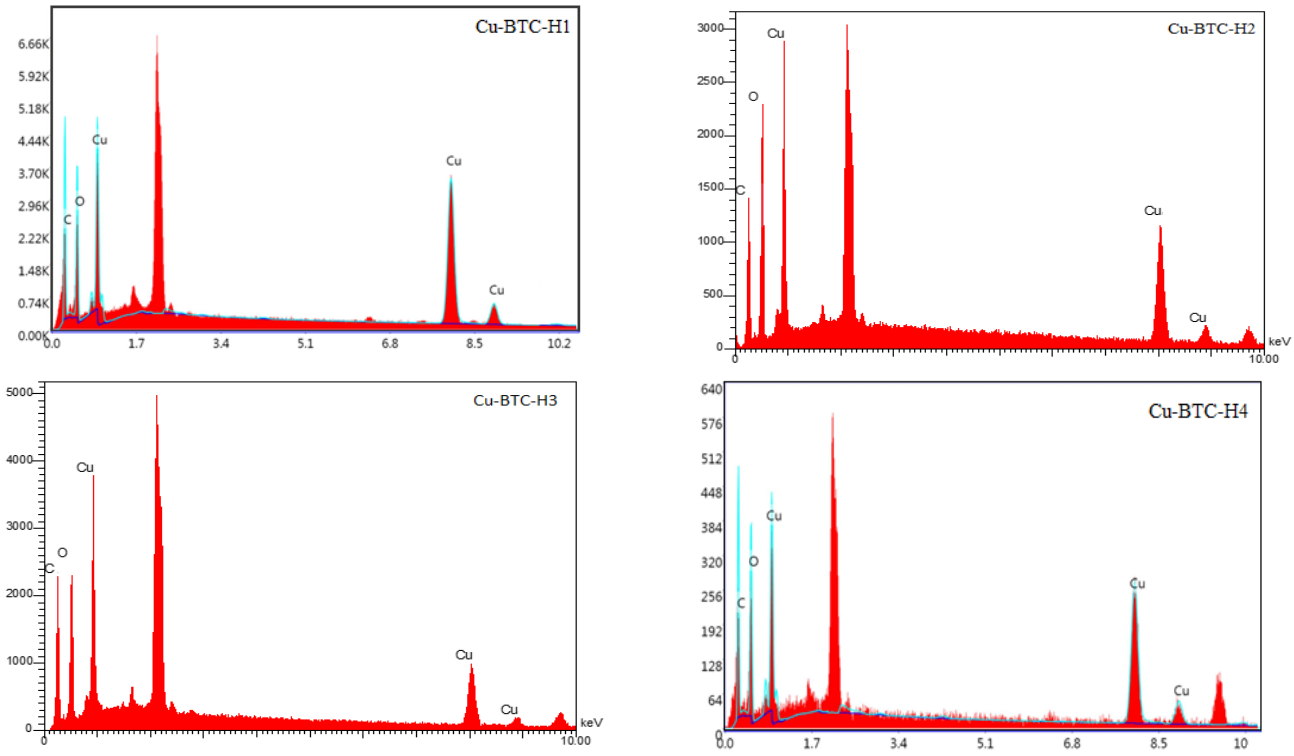

Fig. 5. EDX spectra of the synthesized Cu-BTC samples at different metal-to-ligand molar ratios.

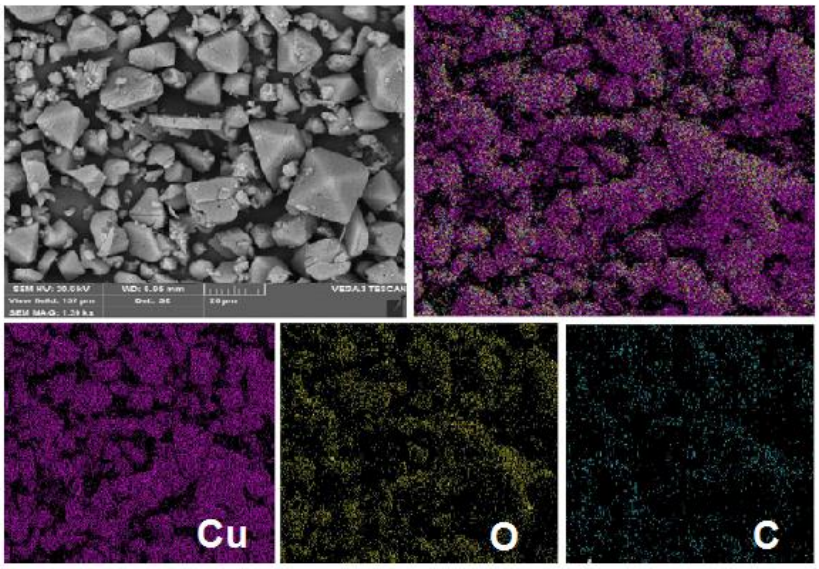

Fig. 6. A typical elemental mapping image of the Cu-BTC-H4 sample.

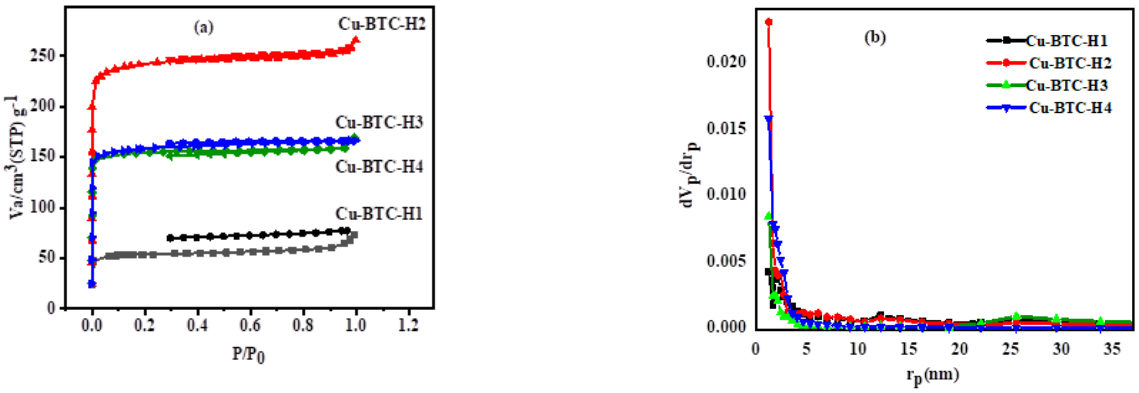

Fig. 7. (a) Nitrogen adsorption-desorption isotherms and (b) BJH analysis of the synthesized Cu-BTC samples at different metal-to-ligand molar ratios.

3.2. Effect of solvent composition

Using different solvent compositions of ethanol/DI-water and ethanol/DI-water/DMF, respectively, the samples Cu-BTC-H2 and Cu-BTC-H5 were synthesized. The XRD patterns of these samples are shown in Figure 8a. The crystal structures of both samples are almost identical. However, the diffraction peaks are more intense and sharper in the case of the Cu-BTC-H5 sample; this indicates its higher crystalline quality and slightly higher crystallite size (49.8 nm) than the Cu-BTC-H2 sample. The crystalline properties of these samples are reported in Table 2, which indicates a little shift of the (222) diffraction peak for the Cu-BTC-H5 sample compared to Cu-BTC-H2, which leads to a small decrease in d-spacing of the (222) planes and a minor increase in its lattice strain. In Figure 8b, the FTIR spectra of Cu-BTC-H2 and Cu-BTC-H5 are compared. The main absorption bands are similar, confirming their similar chemical structure, and it can be concluded that the presence of DMF in the solvent composition did not induce any important and observable effect on the chemical bond configuration of the synthesized Cu-BTC samples.

Figs. 9a and 9b show the microcrystal shapes of Cu-BTC-H2 and Cu-BTC-H5 samples, respectively, for comparison. The Cu-BTC-H2 sample involves spherical, octahedral, and polyhedral shapes with a size of ~15.42 µm. While the Cu-BTC-H5 sample exhibits a mixture of polyhedral and irregular particles, and their sizes are in the range of ~17.25 µm. Therefore, the determining effect of the solvent composition on the morphology of the formed Cu-BTC particles can be verified. This morphology-controlling effect of solvent content is in consistent with previous research such as the one published by Hwang et al. a significant influence of adding methanol to DMF in the solvent on the morphological properties of MOF $\{Zn_2(bdc)_2dabco\}_n$ (ZBD) synthesized by the solvothermal method [16]. Also, Sanil et al. studied the effects of several solvents, such as methanol, ethanol, ethylene glycol, and triethylene glycol, on the size and morphology of Cu-BTC particles, which were synthesized with the assistance of a microwave [56]. In addition, Jang et al. have synthesized ZIF-67 and ZIF-8 particles with different shapes, including polyhedron, sheets, rods, and belt particles by controlling the content of two solvents, ethanol, water, and their combinations [57].

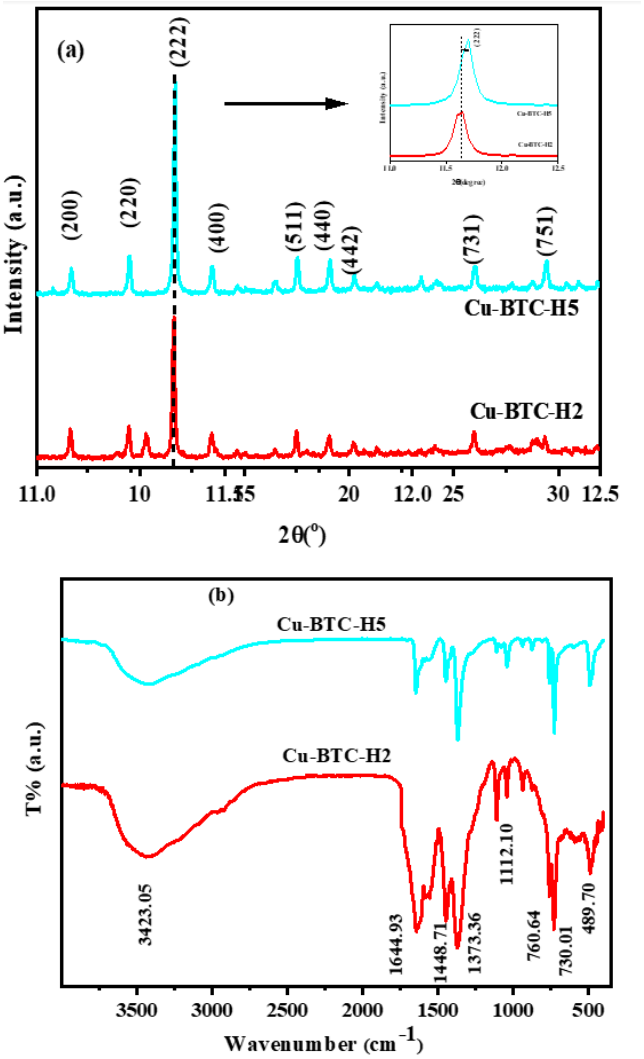

Fig. 8. (a) XRD patterns and (b) FTIR spectra of Cu-BTC-H2 and Cu-BTC-H5 samples synthesized using different solvents.

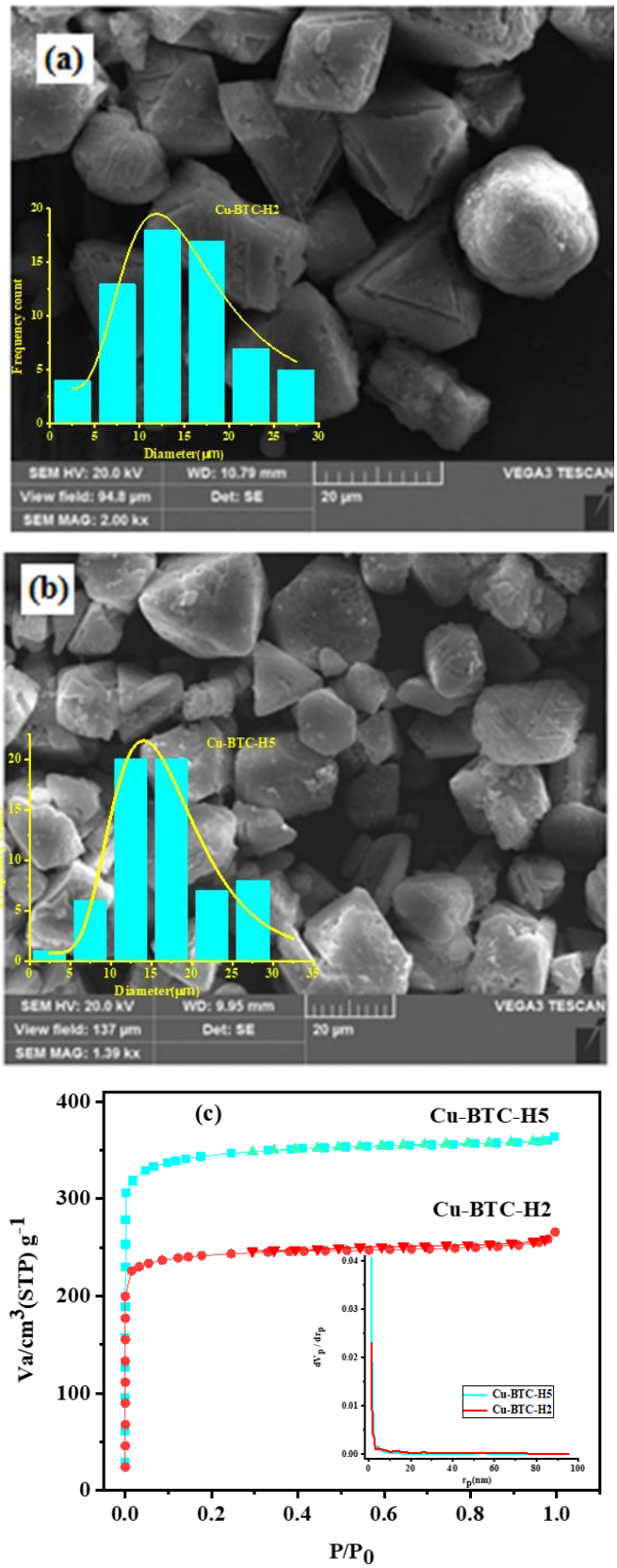

Fig. 9. FESEM image and size distribution histogram of (a) Cu-BTC-H2, (b) Cu-BTC-H5 samples, and (c) Nitrogen adsorption-desorption isotherms and BJH analysis of the Cu-BTC samples with changing solvent composition.

The XRD pattern and FESEM image mentioned above show that the Cu-BTC structure is successfully formed, as can be seen from the variation in the solvent type and metal-to-ligand molar ratios in them. Figure 9c demonstrates that Cu-BTC-H5 has a SSA of 1364.8 m^2g^{-1} and a total pore volume of 0.561 cm^3g^{-1}, which have significant changes compared to Cu-BTC-H2 (with total pore volume of 0.41 cm^3g^{-1} and SSA of 969.5 m^2g^{-1}). However, according to the distribution diagram of the pore from the BJH method, the average pore diameter did not change visibly. So, the structure has become much more porous by changing the solvent, and the volume of its pores has also increased. Hao et al. have synthesized the Cu-BTC with an ethanol and DMF solvent mixture by changing the metal-to-ligand molar ratio to the optimal amount of 1:1, which obtained a large SSA (1644 m^2g^{-1}) and a good structure with at least CuO and Cu_2O impurities [58]. This indicates that regulating the solvent content probably allows more metal clusters and ligands to form the framework leading to improving the generated Cu-BTC structure's SSA and pore volume.

4. Conclusion

In this work, micro-particles of Cu-BTC MOF were synthesized by the solvothermal method, and the effect of the molar ratio of metal-to-ligand and solvent composition on the crystal structure, chemical bond, morphology, and porosity properties of the product were thoroughly investigated. By choosing a different metal-to-ligand molar ratio, four coordination networks were successfully synthesized by the solvothermal method at 120°C for 16 hours. The characterization results verified that the morphology, crystalline quality, and SSA of the synthesized Cu-BTC structures change with the reduction of the metal-to-ligand molar ratio so that the Cu-BTC-H2 sample (with a 1:1 metal-to-ligand molar ratio) exhibited crystallinity of 75% and the highest SSA of 969.5 m^2g^{-1} among other samples. In addition, it was found that changing the solvent composition from DI-water/ethanol to DI-water/ethanol/DMF could significantly enhance the SSA (by 41%) of the product and a crystallinity of 80% was achieved. The effect of DMF addition in the solvent content on the growth mechanism of Cu-BTC was presented and discussed according to the present results and other reported works. According to our systematic study, a mesoporous metal-organic framework (Cu-BTC-H5) with a high SSA and total pore volume of 1364.8 m^2g^{-1} and 0.561 cm^3g^{-1} respectively, was obtained at a metal-to-ligand molar ratio of 1:1 and using a mixture of DI-water/ethanol/DMF as solvents. The results verified the important impact of the studied synthesis parameters for controlling Cu-BTC critical properties for some applications such as sensors, gas storage, and absorption.

Acknowledgements

There is nothing to acknowledgement.

Conflicts of Interest

The author declares that there is no conflict of interest regarding the publication of this article.

References

[1] Li, B., Wen, H.M., Cui, Y., Zhou, W., Qian, G. and Chen, B., 2016. Emerging multifunctional metal–organic framework materials. *Advanced Materials*, *28*(40), pp.8819-8860.

[2] Allendorf, M.D. and Stavila, V., 2015. Crystal engineering, structure–function relationships, and the future of metal–organic frameworks. *CrystEngComm*, *17*(2), pp.229-246.

[3] Salehi, S. and Karimzadeh, I., 2023. A Graphene and Nickel-Cobalt Metal Organic Framework Composite as a high-performance electrode material for supercapacitor application. *Progress in Physics of Applied Materials*, *3*(2), pp.211-216.

[4] Zhang, C.Y., Wang, M.Y., Li, Q.T., Qian, B.H., Yang, X.J. and Xu, X.Y., 2013. Hydrothermal synthesis, crystal structure, and luminescent properties of two zinc (II) and cadmium (II) 3D metal-organic frameworks. *Zeitschrift für anorganische und allgemeine Chemie*, *639*(5), pp.826-831.

[6] Yuan, F., Xie, J., Hu, H.M., Yuan, C.M., Xu, B., Yang, M.L., Dong, F.X. and Xue, G.L., 2013. Effect of pH/metal ion on the structure of metal–organic frameworks based on novel bifunctionalized ligand 4′-carboxy-4, 2′: 6′, 4″-terpyridine. *CrystEngComm*, *15*(7), pp.1460-1467.

[7] Akhbari, K. and Morsali, A., 2011. Effect of the guest solvent molecules on preparation of different morphologies of ZnO nanomaterials from the [Zn2 (1, 4-bdc) 2 (dabco)] metal-organic framework. *Journal of Coordination Chemistry*, *64*(20), pp.3521-3530.

[8] He, Y.C., Guo, J., Zhang, H.M., Ma, J.F. and Liu, Y.Y., 2014. Tuning the void volume in a series of isomorphic porous metal–organic frameworks by varying the solvent size and length of organic ligands. *CrystEngComm*, *16*(24), pp.5450-5457.

[9] Mazaj, M., Birsa Čelič, T., Mali, G., Rangus, M., Kaucic, V. and Zabukovec Logar, N., 2013. Control of the crystallization process and structure dimensionality of Mg–Benzene–1, 3, 5-tricarboxylates by tuning solvent composition. *Crystal growth & design*, *13*(8), pp.3825-3834.

[10] Xia, Z.X., Huang, K.L., Rong, X., Chen, S.C., He, M.Y. and Chen, Q., 2022. Metal-to-ligand ratio-controlled assembly of two Ca (II) complexes: Synthesis, structures, reactant-induced reversible transformation, and catalytic properties. *Inorganic Chemistry Communications*, *145*, p.109906.

[11] Liu, Y., Qi, Y., Su, Y.H., Zhao, F.H., Che, Y.X. and Zheng, J.M., 2010. Five novel cobalt coordination polymers: effect of metal–ligand ratio and structure characteristics of flexible bis (imidazole) ligands. *CrystEngComm*, *12*(10), pp.3283-3290.

[12] McKellar, S.C., Graham, A.J., Allan, D.R., Mohideen, M.I.H., Morris, R.E. and Moggach, S.A., 2014. The effect of pressure on the post-synthetic modification of a nanoporous metal–organic framework. *Nanoscale*, *6*(8), pp.4163-4173.

[13] Cao, Y., Ma, Y., Wang, T., Wang, X., Huo, Q. and Liu, Y., 2016. Facile fabricating hierarchically porous metal–organic frameworks via a template-free strategy. *Crystal Growth & Design*, *16*(1), pp.504-510.

[14] Soni, S., Bajpai, P.K. and Arora, C., 2020. A review on metal-organic framework: Synthesis, properties and application. *Characterization and Application of Nanomaterials*, *3*(2), pp.87-106.

[15] Stock, N. and Biswas, S., 2012. Synthesis of metal-organic frameworks (MOFs): routes to various MOF topologies, morphologies, and composites. *Chemical reviews*, *112*(2), pp.933-969.

[16] Hwang, J., Yan, R., Oschatz, M. and Schmidt, B.V., 2018. Solvent mediated morphology control of zinc MOFs as carbon templates for application in supercapacitors. *Journal of materials chemistry A*, *6*(46), pp.23521-23530.

[17] Troyano, J., Carné-Sánchez, A., Avci, C., Imaz, I. and Maspoch, D., 2019. Colloidal metal–organic framework particles: the pioneering case of ZIF-8. *Chemical Society Reviews*, *48*(23), pp.5534-5546.

[18] Liu, P.P., Cheng, A.L., Yue, Q., Liu, N., Sun, W.W. and Gao, E.Q., 2008. Cobalt (II) coordination networks dependent upon the spacer length of flexible bis (tetrazole) ligands. *Crystal Growth and Design*, *8*(5), pp.1668-1674.

[19] Chui, S.S.Y., Lo, S.M.F., Charmant, J.P., Orpen, A.G. and Williams, I.D., 1999. A chemically functionalizable nanoporous material [Cu3 (TMA) 2 (H2O) 3] n. *Science*, *283*(5405), pp.1148-1150.

[20] Prestipino, C., Regli, L., Vitillo, J.G., Bonino, F., Damin, A., Lamberti, C., Zecchina, A., Solari, P.L., Kongshaug, K.O. and Bordiga, S., 2006. Local structure of framework Cu (II) in HKUST-1 metallorganic framework: spectroscopic characterization upon activation and interaction with adsorbates. *Chemistry of materials*, *18*(5), pp.1337-1346.

[21] Oar-Arteta, L., Wezendonk, T., Sun, X., Kapteijn, F. and Gascon, J., 2017. Metal organic frameworks as precursors for the manufacture of advanced catalytic materials. *Materials Chemistry Frontiers*, *1*(9), pp.1709-1745.

[22] Bacsik, Z., Atluri, R., Garcia-Bennett, A.E. and Hedin, N., 2010. Temperature-induced uptake of CO2 and formation of carbamates in mesocaged silica modified with n-propylamines. *Langmuir*, *26*(12), pp.10013-10024.

[23] Davydovskaya, P., Pohle, R., Tawil, A. and Fleischer, M., 2013. Work function based gas sensing with Cu-BTC metal-organic framework for selective aldehyde detection. *Sensors and Actuators B: Chemical*, *187*, pp.142-146.

[24] Davydovskaya, P., Tawil, A. and Pohle, R., 2014. Ethanol sensing with Cu-BTC Metal Organic Framework: mass sensitive, work function based and IR investigations. *Key Engineering Materials*, *605*, pp.87-90.

[25] Singh, N., Dalakoti, S., Wamba, H.N., Chauhan, R., Divekar, S. and Dasgupta, S., 2023. Preparation of Cu-BTC MOF extrudates for CH4 separation from CH4/N2 gas mixture. *Microporous and Mesoporous Materials*, *360*, p.112723.

[26] Kim, J., Cho, H.Y. and Ahn, W.S., 2012. Synthesis and adsorption/catalytic properties of the metal organic framework CuBTC. *Catalysis Surveys from Asia*, *16*, pp.106-119.

[27] Isaeva, V.I., Saifutdinov, B.R., Chernyshev, V.V., Vergun, V.V., Kapustin, G.I., Kurnysheva, Y.P., Ilyin, M.M. and Kustov, L.M., 2020. Impact of the preparation procedure on the performance of the microporous HKUST-1 metal-organic framework in the liquid-phase separation of aromatic compounds. *Molecules*, *25*(11), p.2648.

[28] He, Y., Zhou, W., Qian, G. and Chen, B., 2014. Methane storage in metal–organic frameworks. *Chemical Society Reviews*, *43*(16), pp.5657-5678.

[29] Isaeva, V.I., Chernyshev, V.V., Sokolova, N.A. and Kapustin, G.I., 2018. Modifying the hydrophobic properties of metal–organic framework HKUST-1. *Russian Journal of Physical Chemistry A*, *92*, pp.2391-2395.

[30] Klimakow, M., Klobes, P., Thunemann, A.F., Rademann, K. and Emmerling, F., 2010. Mechanochemical synthesis of metal− organic frameworks: a fast and facile approach toward quantitative yields and high specific surface areas. *Chemistry of Materials*, *22*(18), pp.5216-5221.

[31] Głowniak, S., Szczęśniak, B., Choma, J. and Jaroniec, M., 2021. Mechanochemistry: Toward green synthesis of metal–organic frameworks. *Materials Today*, *46*, pp.109-124.

[32] Khan, N.A., Haque, E. and Jhung, S.H., 2010. Rapid syntheses of a metal–organic framework material Cu 3 (BTC) 2 (H 2 O) 3 under microwave: a quantitative analysis of accelerated syntheses. *Physical Chemistry Chemical Physics*, *12*(11), pp.2625-2631.

[33] Schlesinger, M., Schulze, S., Hietschold, M. and Mehring, M., 2010. Evaluation of synthetic methods for microporous metal–organic frameworks exemplified by the competitive formation of [Cu2 (btc) 3 (H2O) 3] and [Cu2 (btc)(OH)(H2O)]. *Microporous and Mesoporous Materials*, *132*(1-2), pp.121-127.

[34] Chen, Y., Mu, X., Lester, E. and Wu, T., 2018. High efficiency synthesis of HKUST-1 under mild conditions with high BET surface area and CO2 uptake capacity. *Progress in Natural Science: Materials International*, *28*(5), pp.584-589.

[35] Deyko, G.S., Glukhov, L.M., Isaeva, V.I., Chernyshev, V.V., Vergun, V.V., Archipov, D.A., Kapustin, G.I., Tkachenko, O.P., Nissenbaum, V.D. and Kustov, L.M., 2022. Modifying HKUST-1 crystals for selective ethane adsorption using ionic liquids as synthesis media. *Crystals*, *12*(2), p.279.

[36] Campagnol, N., Van Assche, T.R., Li, M., Stappers, L., Dincă, M., Denayer, J.F., Binnemans, K., De Vos, D.E. and Fransaer, J., 2016. On the electrochemical deposition of metal–organic frameworks. *Journal of Materials Chemistry A*, *4*(10), pp.3914-3925.

[37] Varsha, M.V. and Nageswaran, G., 2020. Direct electrochemical synthesis of metal organic frameworks. *Journal of The Electrochemical Society*, *167*(15), p.155527.

[38] Kaur, R., Kaur, A., Umar, A., Anderson, W.A. and Kansal, S.K., 2019. Metal organic framework (MOF) porous octahedral nanocrystals of Cu-BTC: Synthesis, properties and enhanced adsorption properties. *Materials Research Bulletin*, *109*, pp.124-133.

[39] Biemmi, E., Christian, S., Stock, N. and Bein, T., 2009. High-throughput screening of synthesis parameters in the formation of the metal-organic frameworks MOF-5 and HKUST-1. *Microporous and Mesoporous Materials*, *117*(1-2), pp.111-117.

[40] Mote, V.D., Purushotham, Y. and Dole, B.N., 2012. Williamson-Hall analysis in estimation of lattice strain in nanometer-sized ZnO particles. *Journal of theoretical and applied physics*, *6*, pp.1-8.

[41] Suryanarayana, C., Norton, M.G., Suryanarayana, C. and Norton, M.G., 1998. *X-rays and Diffraction* (pp. 3-19). Springer US.

[42] Salehi, S., Aghazadeh, M. and Karimzadeh, I., 2022. Zn-MOF electrode material for supercapacitor applications. *Progress in Physics of Applied Materials*, *2*(1), pp.77-82.

[43] Yang, F., Hu, W., Yang, C., Patrick, M., Cooksy, A.L., Zhang, J., Aguiar, J.A., Fang, C., Zhou, Y., Meng, Y.S. and Huang, J., 2020. Tuning internal strain in metal–organic frameworks via vapor phase infiltration for CO2 reduction. *Angewandte Chemie*, *132*(11), pp.4602-4610.

[44] Lopez-Rubio, A., Flanagan, B.M., Gilbert, E.P. and Gidley, M.J., 2008. A novel approach for calculating starch crystallinity and its correlation with double helix content: A combined XRD and NMR study. *Biopolymers: Original Research on Biomolecules*, *89*(9), pp.761-768.

[45] Liu, S., Fu, L.H., Liu, Y.J., Meng, L.Y., Dong, Y.Y., Li, Y.Y. and Ma, M.G., 2016. Cu/C or Cu2O/C composites: selective synthesis, characterization, and applications in water treatment. *Science of Advanced Materials*, *8*(11), pp.2045-2053.

[46] Samuel, M.S., Suman, S., Selvarajan, E., Mathimani, T. and Pugazhendhi, A., 2020. Immobilization of Cu3 (btc) 2 on graphene oxide-chitosan hybrid composite for the adsorption and photocatalytic degradation of methylene blue. *Journal of Photochemistry and Photobiology B: Biology*, *204*, p.111809.

[47] Azad, F.N., Ghaedi, M., Dashtian, K., Hajati, S. and Pezeshkpour, V., 2016. Ultrasonically assisted hydrothermal synthesis of activated carbon–HKUST-1-MOF hybrid for efficient simultaneous ultrasound-assisted removal of ternary organic dyes and antibacterial investigation: Taguchi optimization. *Ultrasonics sonochemistry*, *31*, pp.383-393.

[48] Nehra, M., Kumar, R., Dilbaghi, N. and Kumar, S., 2023. Controlled synthesis of Cu-MOF possessing peroxidase-mimetic activity for the colorimetric detection of tetracycline in aqueous solution. *New Journal of Chemistry*, *47*(16), pp.7595-7603.

[49] Shen, T., Liu, T., Mo, H., Yuan, Z., Cui, F., Jin, Y. and Chen, X., 2020. Cu-based metal–organic framework HKUST-1 as effective catalyst for highly sensitive determination of ascorbic acid. *Rsc Advances*, *10*(39), pp.22881-22890.

[50] Ghafuri, H., Ganjali, F. and Hanifehnejad, P., 2020. Cu. BTC MOF as a novel and efficient catalyst for the synthesis of 1, 8-dioxo-octa-hydro xanthene. *Chemistry Proceedings*, *3*(1).

[51] Lin, S., Song, Z., Che, G., Ren, A., Li, P., Liu, C. and Zhang, J., 2014. Adsorption behavior of metal–organic frameworks for methylene blue from aqueous solution. *Microporous and mesoporous materials*, *193*, pp.27-34.

[52] Kim, K., Kim, S., Lee, H.N., Park, Y.M., Bae, Y.S. and Kim, H.J., 2019. Electrochemically derived CuO nanorod from copper-based metal-organic framework for non-enzymatic detection of glucose. *Applied Surface Science*, *479*, pp.720-726.

[53] Liu, Y., Ghimire, P. and Jaroniec, M., 2019. Copper benzene-1, 3, 5-tricarboxylate (Cu-BTC) metal-organic framework (MOF) and porous carbon composites as

efficient carbon dioxide adsorbents. *Journal of colloid and interface science*, *535*, pp.122-132.

[54] Luo, Y., Chen, D., Wei, F. and Liang, Z., 2018. Synthesis of Cu-BTC metal-organic framework by ultrasonic wave-assisted ball milling with enhanced congo red removal property. *ChemistrySelect*, *3*(41), pp.11435-11440.

[55] Zhang, J., Zhang, T., Yu, D., Xiao, K. and Hong, Y., 2015. Transition from ZIF-L-Co to ZIF-67: a new insight into the structural evolution of zeolitic imidazolate frameworks (ZIFs) in aqueous systems. *CrystEngComm*, *17*(43), pp.8212-8215.

[56] Sanil, E.S., Cho, K.H., Lee, S.K., Lee, U.H., Ryu, S.G., Lee, H.W., Chang, J.S. and Hwang, Y.K., 2015. Size and morphological control of a metal–organic framework Cu-BTC by variation of solvent and modulator. *Journal of porous materials*, *22*, pp.171-178.

[57] Jang, J.S., Koo, W.T., Kim, D.H. and Kim, I.D., 2018. In situ coupling of multidimensional MOFs for heterogeneous metal-oxide architectures: toward sensitive chemiresistors. *ACS central science*, *4*(7), pp.929-937.

[58] Hao, S. and Liu, Y., 2022. Constructing and synthesizing optimal Cu-BTC and its application in low-temperature denitration. *Journal of Materials Science*, *57*(3), pp.1689-1702.